

34 **Abstract**

35 Hippocampal mossy fibers have long been recognized as conditional detonators owing to
36 prominent short-term facilitation, but the patterns of activity required to fire postsynaptic CA3
37 pyramidal neurons remain poorly understood. We show that mossy fibers count the number of
38 spikes to transmit information to CA3 pyramidal cells through a distinctive interplay between
39 presynaptic calcium dynamics, buffering and vesicle replenishment. This identifies a previously
40 unexplored information coding mechanism in the brain.

41

42 **Main text**

43 Neurons encode and transmit information in the frequency and temporal precision of
44 action potentials (APs) they discharge^{1,2}. Presynaptic terminals are key elements involved in the
45 translation of electrical signals to neurotransmitter release³. During active states, several types of
46 neurons fire in bursts. For example, hippocampal granule cells fire infrequently, but discharge
47 bursts of APs with highly variable frequencies^{4,5}. However, how presynaptic mossy fiber bouton
48 (MFB) terminals decode the frequency and the number of APs in the incoming bursts to transmit
49 information remains poorly understood.

50 We first aimed to determine how AP transmission to CA3 pyramidal cells is encoded by
51 the frequency and the number of APs discharged by granule cells. We recorded CA3 pyramidal
52 cells in current-clamp and stimulated mossy fibers using trains of APs with the initial frequency
53 of the first 5 stimuli delivered at 20 or 100 Hz and the last 3 stimuli fixed at 100 Hz. As expected
54 AP firing by CA3 cells progressively increased during mossy fiber stimulation (**Fig. 1a-c**). The
55 probability of observing the first postsynaptic spike sharply increased at the 6th stimuli (**Fig. 1d**).
56 Both the probability of CA3 pyramidal cell firing at the 6th stimulus and the probability of
57 observing the first AP were independent from the initial burst frequency (**Fig. 1c,d**). This
58 suggests that AP transmission at MFB terminals is mainly determined by the number of spikes
59 within the train and not by the average train frequency. Glutamate release from MFBs is greatly
60 amplified during trains of stimuli⁶⁻⁸, however how the frequency and number of stimuli are
61 translated to specific patterns of glutamate release remains unknown. We varied the burst
62 frequency and the number of stimuli to dissect the contribution of these two parameters. The 6th

63 evoked post synaptic current (EPSC) amplitude in a 5X20 Hz + 1X100 Hz burst was nearly
64 identical to the 6th EPSC amplitude of a pure 100 Hz train (**Fig. 1e,f**). Similarly, the 6th EPSC
65 amplitude of a 5X100 Hz + 1X20 Hz burst closely matched the amplitude of the 6th EPSC in a 20
66 Hz train (**Fig. 1g,h**). This supports the idea that the average frequency of the train is not a
67 determining factor of the rate of glutamate release. Instead, the number of preceding stimuli and
68 the frequency of only the last stimulus appear to dictate the efficiency of synchronous glutamate
69 release at the last 6th spike. These data argue that MFB terminals use a counting logic. We
70 confirmed that such counting logic was observed for any stimulus number between 2 – 10
71 (**Supplementary Fig. 1a,b**) and for frequencies between 10 and 100 Hz (**Supplementary Fig.**
72 **1c**).

73 To gather insights on the presynaptic determinants of the counting logic, we next
74 performed fast whole-bouton two-photon random-access Ca²⁺ imaging using the low-affinity
75 Ca²⁺ indicator Fluo-4FF to measure the dynamic modulation of presynaptic [Ca²⁺] during AP
76 trains (**Fig. 2**). We found that the amplitude of AP-evoked Ca²⁺-fluorescence transients remained
77 constant during AP bursts (**Fig. 2b-e**). This indicates that AP-evoked Ca²⁺ influx does not change
78 during 20 Hz or 100 Hz stimulations and therefore, modulation of voltage-gated Ca²⁺ channel
79 (VGCCs) activity is unlikely to contribute to short-term plasticity in MFB terminals. We next
80 explored the presynaptic Ca²⁺ dynamics by direct fitting of the experimental traces using a non-
81 stationary single compartment model^{9,10} (**Fig. 2b,c**, Online Methods). The model, which
82 incorporated three major endogenous Ca²⁺ buffers known to be present in MFBs (calbindin-D_{28K}
83 (CB), calmodulin (CaM), and ATP) provided close fits of the experimental data (**Fig. 2b,c** and
84 **Supplementary Fig. 2**). It is noteworthy that a similar model with a single fast high affinity
85 endogenous buffer¹¹ could not replicate the Ca²⁺ imaging data (**Supplementary Fig. 3**). The
86 fitting allowed us to estimate Ca²⁺ removal rate in our experimental conditions (k_{rem} range 0.2 -
87 0.7 ms⁻¹), which was in close agreement with previous estimates obtained with high affinity Ca²⁺
88 indicator Fluo-4⁹.

89 To understand whether the interplay between presynaptic Ca²⁺ dynamics and endogenous
90 Ca²⁺ buffering can lead to AP counting, we performed quantitative modelling of AP-evoked Ca²⁺
91 influx, buffering and diffusion, and glutamate release in MFBs. The three-dimensional model
92 incorporated key ultrastructural and functional properties of MFBs including multiple release

93 sites, experimentally constrained presynaptic Ca^{2+} dynamics and loose coupling between VGCCs
94 and vesicular release sensors^{9,11-13} (**Fig. 3a** and Online Methods). The simulation unit, which
95 represented a part of MFB with a single release site, was modelled as a parallelepiped of size 0.5
96 $\mu\text{m} \times 0.5 \mu\text{m} \times 0.79 \mu\text{m}$ with a single VGCC cluster in the middle of the bottom base (**Fig. 3a**).
97 As in the case of the single compartment model we assumed the presence of three major MFB
98 endogenous Ca^{2+} buffers: CB, ATP and CaM. At physiological conditions CaM is known to be
99 distributed between membrane-bound and mobile states, and this distribution is regulated by
100 intracellular $[\text{Ca}^{2+}]$ ¹⁴⁻¹⁶. We first considered a limiting case of ‘Mobile CaM’ model. We
101 simulated spatial MFB Ca^{2+} dynamics in response to bursts of APs and used the obtained $[\text{Ca}^{2+}]$
102 transients at the release site (90 nm away from the VGCC cluster, (**Fig. 3b**) to perform
103 simulations of vesicular release using a Monte Carlo implementation of Ca^{2+} -activated vesicle
104 fusion model¹² (**Fig. 3c** and **Supplementary Fig. 4**). To account for vesicle replenishment during
105 AP bursts we included a vesicle replenishment step in the model and experimentally constrained
106 the replenishment rate constant ($k_{rep} = 20 \text{ s}^{-1}$) (**Supplementary Fig. 5**). We found that ‘Mobile
107 CaM’ model indeed replicated the AP counting during mixed 20 Hz and 100 Hz AP trains (**Fig.**
108 **3d,e** and **Supplementary Fig. 6**). What mechanisms underlie the counting logic? The model
109 predicted that the peak values of Ca^{2+} transients ($[\text{Ca}^{2+}]_{peak}$) were gradually augmented during
110 AP bursts which was mainly attributed to the increase in residual $[\text{Ca}^{2+}]_{residual}$ and was mostly
111 independent of the stimulation frequency (**Fig. 3b**). This argues that EPSC facilitation predicted
112 by ‘Mobile CaM’ model was due to $[\text{Ca}^{2+}]_{residual}$ accumulation and not due to endogenous Ca^{2+}
113 buffer saturation (which normally leads to a progressive increase of the amplitudes of individual
114 AP-evoked Ca^{2+} transients $[\text{Ca}^{2+}]_{amp} = [\text{Ca}^{2+}]_{peak} - [\text{Ca}^{2+}]_{residual}$ ¹³). Indeed, the model revealed that
115 fast and low affinity CaM N-lobe did not show progressive saturation. However, slower and high
116 affinity buffers CB and CaM C-lobe did saturate during AP bursts (**Supplementary Fig. 7**). This
117 at first sight contradictory observation was fully in line with the dominant effect of CaM N-lobe
118 on release site Ca^{2+} dynamics and vesicle fusion¹⁴ (**Supplementary Fig. 8**).

119 Although ‘Mobile CaM’ model replicated AP counting the overall level of EPSC
120 facilitation predicted by this model was $\sim 40\%$ lower than the experimentally observed values
121 (**Fig. 1f, h**). Therefore, we considered another limiting case, ‘CaM dislocation’ model. In this
122 model (described in detail in our previous publication¹⁴) we considered that CaM was initially

123 bound to the presynaptic membrane via interaction of its C-lobe with neuromodulin and with
124 other IQ-motif presynaptic membrane proteins (e.g. VGCCs)¹⁴⁻¹⁶. The model assumed that Ca²⁺
125 binding by the CaM C-lobe during AP bursts led to dissociation of CaM from its membrane
126 binding partners and thus resulted in a stimulation-dependent reduction of Ca²⁺ buffering
127 capacity in the AZ (**Fig. 3f**). This in turn led to progressive increase of [Ca²⁺] transients at the
128 AZ (**Fig. 3g**) and to facilitation of EPSCs (**Fig. 3h**). The progressive reduction of AZ Ca²⁺
129 buffering capacity predicted by the model did not depend on the frequency of AP bursts. Thus,
130 ‘CaM dislocation’ model also supported the counting logic at MFB terminals. In contrast to
131 ‘Mobile CaM’ model the dislocation model predicted substantial increase of AP-evoked
132 [Ca²⁺]_{amp} at the release site which resulted in stronger EPSC facilitation (**Fig. 3g,i**). Overall, the
133 experimentally observed level of EPSC facilitation in MFB terminals is likely to be attributed to
134 a joint contribution of the ‘Mobile CaM’ and ‘CaM dislocation’ limiting cases (**Fig. 3i**).
135 Interestingly, the effect of somewhat stronger augmentation of [Ca²⁺]_{peak} on vesicular release at
136 higher frequencies was compensated in both models by the lower vesicle occupancy at the
137 release site during high frequency stimulation (**Supplementary Fig. 10**). This indicates that
138 frequency-dependent differences in release site occupancy also contribute to the counting logic
139 behavior of MFBs.

140 We aimed to understand how granule cells generate CA3 pyramidal cells firing, the first
141 relay of information in the hippocampus¹⁷. This question is important because discharge of a
142 single AP by a single CA3 pyramidal cell has dramatic network consequences such as initiation
143 of sharp-wave ripples¹⁸. We demonstrate that MFB count the number of spikes to transmit
144 information to CA3 pyramidal cells independently of the average spike frequency. Our results
145 argue that MFB counting logic can be explained by (i) accumulation of [Ca²⁺]_{residual} which is
146 largely independent of stimulation frequency due to relatively slow Ca²⁺ removal rate k_{rem} ; (ii)
147 loose coupling between VGCCs and vesicular release sensors which leads to moderate changes
148 of [Ca²⁺]_{peak} at release site (in the range of 10 μM - 15μM) that is efficiently modulated by
149 changes in [Ca²⁺]_{residual} (~ 2 μM); (iii) the dominant role of CaM N-lobe on fast Ca²⁺ buffering at
150 the release sites; (iv) possible contribution of stimulation-dependent reduction of Ca²⁺ buffering
151 capacity in the AZ due to CaM dislocation, and; (v) more efficient vesicle replenishment at lower
152 frequencies. All of the above elements are uniquely combined in MFBs to allow AP counting, an

153 information coding strategy which contrasts rate and temporal coding described in other types of
154 synapses².

155 Bibliography

- 156 1 Adrian, E. D. & Zotterman, Y. The impulses produced by sensory nerve-endings: Part II.
157 The response of a Single End-Organ. *The Journal of physiology* **61**, 151-171 (1926).
- 158 2 Stein, R. B., Gossen, E. R. & Jones, K. E. Neuronal variability: noise or part of the
159 signal? *Nature reviews. Neuroscience* **6**, 389-397, doi:10.1038/nrn1668 (2005).
- 160 3 Del Castillo, J. & Katz, B. Quantal components of the end-plate potential. *The Journal of*
161 *physiology* **124**, 560-573 (1954).
- 162 4 Pernia-Andrade, A. J. & Jonas, P. Theta-gamma-modulated synaptic currents in
163 hippocampal granule cells in vivo define a mechanism for network oscillations. *Neuron*
164 **81**, 140-152, doi:10.1016/j.neuron.2013.09.046 (2014).
- 165 5 Pilz, G. A. *et al.* Functional Imaging of Dentate Granule Cells in the Adult Mouse
166 Hippocampus. *The Journal of neuroscience : the official journal of the Society for*
167 *Neuroscience* **36**, 7407-7414, doi:10.1523/JNEUROSCI.3065-15.2016 (2016).
- 168 6 Toth, K., Soares, G., Lawrence, J. J., Philips-Tansey, E. & McBain, C. J. Differential
169 mechanisms of transmission at three types of mossy fiber synapse. *The Journal of*
170 *neuroscience : the official journal of the Society for Neuroscience* **20**, 8279-8289 (2000).
- 171 7 Chamberland, S., Evstratova, A. & Toth, K. Interplay between Synchronization of
172 Multivesicular Release and Recruitment of Additional Release Sites Support Short-Term
173 Facilitation at Hippocampal Mossy Fiber to CA3 Pyramidal Cells Synapses. *The Journal*
174 *of neuroscience : the official journal of the Society for Neuroscience* **34**, 11032-11047,
175 doi:10.1523/JNEUROSCI.0847-14.2014 (2014).
- 176 8 Salin, P. A., Scanziani, M., Malenka, R. C. & Nicoll, R. A. Distinct short-term plasticity
177 at two excitatory synapses in the hippocampus. *Proceedings of the National Academy of*
178 *Sciences of the United States of America* **93**, 13304-13309 (1996).
- 179 9 Scott, R. & Rusakov, D. A. Main determinants of presynaptic Ca²⁺ dynamics at
180 individual mossy fiber-CA3 pyramidal cell synapses. *The Journal of neuroscience : the*
181 *official journal of the Society for Neuroscience* **26**, 7071-7081,
182 doi:10.1523/JNEUROSCI.0946-06.2006 (2006).
- 183 10 Ermolyuk, Y. S. *et al.* Differential triggering of spontaneous glutamate release by P/Q-,
184 N- and R-type Ca²⁺ channels. *Nature neuroscience* **16**, 1754-1763, doi:10.1038/nn.3563
185 (2013).
- 186 11 Bischofberger, J., Geiger, J. R. & Jonas, P. Timing and efficacy of Ca²⁺ channel
187 activation in hippocampal mossy fiber boutons. *The Journal of neuroscience : the official*
188 *journal of the Society for Neuroscience* **22**, 10593-10602 (2002).
- 189 12 Lou, X., Scheuss, V. & Schneggenburger, R. Allosteric modulation of the presynaptic
190 Ca²⁺ sensor for vesicle fusion. *Nature* **435**, 497-501, doi:10.1038/nature03568 (2005).
- 191 13 Vyleta, N. P. & Jonas, P. Loose coupling between Ca²⁺ channels and release sensors at a
192 plastic hippocampal synapse. *Science* **343**, 665-670, doi:10.1126/science.1244811
193 (2014).
- 194 14 Timofeeva, Y. & Volynski, K. E. Calmodulin as a major calcium buffer shaping vesicular
195 release and short-term synaptic plasticity: facilitation through buffer dislocation.
196 *Frontiers in cellular neuroscience* **9**, 239, doi:10.3389/fncel.2015.00239 (2015).

- 197 15 Kumar, V. *et al.* Structural basis for the interaction of unstructured neuron specific
198 substrates neuromodulin and neurogranin with Calmodulin. *Scientific reports* **3**, 1392,
199 doi:10.1038/srep01392 (2013).
- 200 16 Alexander, K. A., Wakim, B. T., Doyle, G. S., Walsh, K. A. & Storm, D. R.
201 Identification and characterization of the calmodulin-binding domain of neuromodulin, a
202 neurospecific calmodulin-binding protein. *The Journal of biological chemistry* **263**,
203 7544-7549 (1988).
- 204 17 Andersen, P., Bliss, T. V. & Skrede, K. K. Lamellar organization of hippocampal
205 pathways. *Experimental brain research* **13**, 222-238 (1971).
- 206 18 Bazelot, M., Telenczuk, M. T. & Miles, R. Single CA3 pyramidal cells trigger sharp
207 waves in vitro by exciting interneurons. *The Journal of physiology*,
208 doi:10.1113/JP271644 (2016).

209

210

211

212

213

214

215

216

217

218

219

220

221

222

223

224

225

226

227 **Figure Legends**

228 **Figure 1 – Transmission of information to CA3 pyramidal cells depends on the number of** 229 **APs in bursts**

230 (a) Representative current-clamp recordings from a CA3 pyramidal cell. The red arrows point to
231 the 6th stimulus in the trains where postsynaptic AP probability increased sharply. (b, c) CA3
232 pyramidal cell firing probability as a function of time (b) and of the number of APs (c) during
233 two stimulation paradigms. (d) Probability of observing the first AP. Both AP probability and the
234 probability of observing the first AP are mainly determined by the number of preceding APs but
235 not by the average burst frequency (b-d, n = 5 cells). (e-h) Analysis of short-term facilitation at
236 MFBs. (e,g) Representative trains of EPSCs recorded using indicated stimulation paradigms.
237 Gray traces, single trials; black traces, the averages of 20 trials. (f,h) Summary graphs showing
238 average EPSC amplitude as a function of time (n = 19 for 20 Hz; n = 15 for 5X20 Hz + 1X100
239 Hz; n = 25 for 100 Hz; n = 10 for 5X100 Hz+ 1X20 Hz).

240

241 **Figure 2 – Ca²⁺ dynamics in MFB terminals**

242 (a) Montage of multiple two-photon Z-stack maximal projections showing the axon anatomy of a
243 typical granule cell filled with a morphological tracer AlexaFluor 594. The intact axon was
244 followed to the CA3 region, where it formed giant MFB terminals (insets). (b,c) Representative
245 measurements of Ca²⁺ dynamics in two MFBs. Left, bouton morphology, dots indicate recording
246 positions for random-access two-photon Ca²⁺ imaging. Middle, corresponding whole bouton
247 Ca²⁺ Fluo-4FF fluorescence elevations in response to 20 Hz and 100 Hz AP stimulations (black
248 traces, average of 140 and 133 sweeps, respectively). The red curves represent the non-stationary
249 single compartment model fit corresponding to $\Delta[\text{Ca}^{2+}]_{\text{total}} = 33.3 \mu\text{M}$, model-predicted values of
250 k_{rem} are shown for each bouton. Right, corresponding AP-evoked whole-bouton [Ca²⁺]
251 transients computed using the non-stationary model. (d) Normalized peak amplitude of AP-
252 evoked Fluo-4FF fluorescence as a function of AP number (n = 7 MFBs for both 20 Hz and 100
253 Hz stimulation).

254

255 **Figure 3 – Modelling of evoked presynaptic Ca^{2+} dynamics and vesicular release reveals a**
256 **plausible mechanism for AP counting logic in MFB terminals.**

257 (a) Left, geometry of a parallelepiped-shaped modelling unit ($0.5 \mu\text{m} \times 0.5 \mu\text{m} \times 0.79 \mu\text{m}$) used
258 in VCell simulations representing part of a MFB containing a single active zone (AZ) with a 40
259 nm x 80 nm VGCC cluster, overlaid with a representative electron microscopy image that
260 depicts part of a MFB with a single AZ (see Online methods for details). Right, snapshots of
261 VCell-computed spatial $[\text{Ca}^{2+}]$ profiles in the central XZ modelling unit plane during 6X100 Hz
262 AP stimulation in the limiting case of ‘Mobile CaM’ model. (b) Left, VCell-computed $[\text{Ca}^{2+}]$
263 transients at the release site located at $d = 90 \text{ nm}$ away from the VGCC cluster during 6X100 Hz
264 and 5X20 + 1X100 AP trains. Right, plot of corresponding residual ($[\text{Ca}^{2+}]_{\text{residual}}$) and peak
265 ($[\text{Ca}^{2+}]_{\text{peak}}$) before and after each AP in the trains (c) Schematics of the modified allosteric model
266 of Ca^{2+} -driven vesicle release and replenishment¹². (d) Simulated EPSCs, average of $M =$
267 60,000 Monte Carlo runs for each paradigm scaled for RRP of size $m = 125$. (e) Summary graph
268 showing simulated EPSC amplitude as a function of time for the two stimulation paradigms
269 shown in (d). (f) Snapshots of spatial distribution of normalized total [CaM] (which accounts for
270 all CaM molecules irrespective of their Ca^{2+} binding state) in the AZ plane, illustrating
271 progressive dislocation of CaM from the membrane during AP stimulation predicted by ‘CaM
272 dislocation model’¹⁴ (see Online methods for details). (g) VCell-computed $[\text{Ca}^{2+}]$ transients at
273 the release site during 6X100 Hz and 5X20 Hz + 1X100 Hz AP trains and (h) corresponding
274 simulated EPSCs for the case of ‘CaM dislocation’ model. (i) Summary graph showing that
275 experimentally observed short-term facilitation levels are likely to be explained by joint
276 contribution of the two limiting cases represented by ‘Mobile CaM’ (low facilitation) and by
277 ‘CaM dislocation’ (high facilitation) models that both allow AP counting logic.

278

279

280

281

282

283 **Online Methods**

284 *Hippocampal slice preparation*

285 Experiments involving the use of animals were performed in accordance with guidelines
286 provided by the Animal Protection Committee of Laval University. Acute hippocampal slices
287 from P17 – P25 male rats were prepared according to accepted procedures⁷. First, the animals
288 were anesthetized with isoflurane. The brain was extracted and immersed in an oxygenated
289 cutting ACSF solution maintained at 4 °C. The cutting ACSF solution contained (in mM): NaCl
290 87, NaHCO₃ 25, KCl 2.5, NaH₂PO₄ 1.25, MgCl₂ 7, CaCl₂ 0.5, glucose 25 and sucrose 75 (pH =
291 7.4, 330 mOsm). The brain was then dissected according to instructions for optimal preservation
292 of the hippocampal mossy fibers¹⁹. The brain hemispheres were glued on the specimen disk of a
293 Leica VT1000S vibratome and submerged in cutting ACSF solution. Slices (300 µm) were cut
294 and transferred to an oxygenated and heated (32 °C) ACSF solution containing (in mM): NaCl
295 124, NaHCO₃ 25, KCl 2.5, MgCl₂ 2.5, CaCl₂ 1.2 and glucose 10 (pH = 7.4, 300 mOsm). Slices
296 were left to recover for 30 minutes at 32 °C. Slices were then left at room temperature.
297 Experiments were started one hour after the slicing procedure.

298

299 *Whole-cell patch-clamp recording*

300 Hippocampal slices were maintained under a nylon mesh in a recording chamber under an
301 upright microscope. The slice was perfused with oxygenated warmed recording ACSF solution,
302 containing (in mM): NaCl 124, NaHCO₃ 25, KCl 2.5, MgCl₂ 2.5, CaCl₂ 1.2 and glucose 10. The
303 solution was oxygenated by bubbling a gas mixture composed of 95% O₂ and 5% CO₂.
304 Temperature was maintained at 32 ± 1 °C throughout all experiments. The perfusion rate was
305 adjusted to a constant 2 ml/min. Visually-guided whole-cell patch-clamp recordings were
306 obtained from CA3 pyramidal cells with a solution containing: K-gluconate 120, KCl 20,
307 HEPES 10, MgCl₂ 2, Mg₂ATP 2, NaGTP 0.3, phosphocreatine 7, EGTA 0.6 (pH = 7.2, 295
308 mOsm). Borosilicate glass electrodes had a resistance of 3 – 5 MΩ for CA3 pyramidal cell
309 recordings. After obtaining a stable whole-cell configuration, CA3 pyramidal cells were held in
310 voltage-clamp or in current-clamp. Voltage-clamp recordings were performed at -70 mV.
311 Current-clamp recordings were performed at the resting membrane potential of the CA3
312 pyramidal cells (-70 ± 5 mV). Minimal stimulation of mossy fibers was performed using an

313 electrode positioned in the stratum lucidum and connected to a constant current stimulus isolator
314 (A360, WPI, Florida, USA). The pipette was gently moved in the stratum lucidum until large,
315 fast and facilitating EPSCs could be recorded. The stimulation intensity was then decreased to
316 achieve conditions in which both failures and successes could be observed. To confirm the
317 mossy fiber identity of the recorded EPSCs or EPSPs, DCG-IV (1 μ M) was applied in the end of
318 a subset of experiments. Recordings in which the postsynaptic response was decreased by at least
319 80% were conserved for further analysis. Electrophysiological data was acquired with Molecular
320 Devices equipment (Axopatch 200B amplifier and Digidata 1322A, or MultiClamp 700B
321 amplifier with Digidata 1440A) and the Clampex suite. The electrophysiological data was low-
322 pass filtered at 2 kHz, digitized at 10 kHz and recorded on a personal computer. For calcium
323 imaging experiments, whole-cell patch-clamp recordings were obtained from granule cells with
324 the solution described above, but lacking EGTA. This patch solution was supplemented with 40
325 μ M of the morphological dye Alexa-594 and 375 μ M of the low-affinity calcium indicator Fluo-
326 4FF. Granule cells were held in the current-clamp mode at their resting membrane potential.
327 Action potentials were evoked by brief current injections (2 ms, 1 – 1.5 nA) in trains of 10 APs,
328 at either 20 Hz or 100 Hz. Glass electrodes used for whole-cell recordings from granule cells had
329 a resistance between 4 – 7 M Ω .

330

331 *Random-access two-photon calcium imaging*

332 Following diffusion for at least 1 hour of the fluorophores in the granule cell, the axon was
333 tracked to the CA3 region^{7,9}. Giant MF boutons were unequivocally identified in the CA3 region
334 based on their morphology imaged with the AlexaFluor-594 fluorescence. 20 sites evenly
335 dispersed on the whole bouton were recorded quasi-simultaneously, yielding an imaging speed
336 of 950 Hz. This recording paradigm allowed a good compromise between signal to noise ratio of
337 the signal and the temporal resolutions, and therefore enabled recording calcium elevations
338 generated by high-frequency firing of APs. The very low-affinity Ca²⁺ indicator Fluo-4FF
339 proved critical to resolve high-frequency bursts of APs evoked at 100 Hz without indicator
340 saturation. We used a custom built random-access two-photon microscope^{7,20}. A two-photon
341 titanium:sapphire laser (Chameleon Ultra II, Coherent) tuned at 800 nm provided the light source
342 (80 MHz, 140 fs pulse width and with an average power >4 W). The laser beam was redirect by
343 a pair of acousto-optic deflectors (AODs; A-A Opto Electronics) to enable random access over

344 the field of view. The laser beam was focused on the brain slice through a high NA water-
345 immersion objective (25X objective, with a NA = 0.95). Transmitted photons passed through a
346 high-numerical aperture oil condenser (NA = 1.4) and were low-pass filtered at 720 nm. Photons
347 were separated by a dichroic mirror (580 nm) to independently collect red and green photons.
348 Photons were then band-pass filtered at 500-560 nm for the green channel and 595-665 nm for
349 the red channel. Both the red and the green photons were collected simultaneously. Collection of
350 photons was performed using a pair of AsGaP photomultiplier tubes (H7422P-40, Hamamatsu)
351 located close to the recording chamber. The laser and the acquisition system were controlled by a
352 Labview custom-made software²⁰.

353

354 *Analysis of electrophysiological and calcium imaging data*

355 Electrophysiological data was analyzed in Clampfit and in Igor Pro. AP probability was
356 calculated from 20 sweeps. To avoid inducing long-term plasticity, sweeps were evoked every
357 30 seconds. EPSC amplitude was measured from the average trace obtained from 20 sweeps.
358 Calcium elevations recorded in giant MF terminals were exported to Excel database. The $\Delta G/G$
359 ratio was calculated for all trials and trials (50 – 140) were averaged together. The peak Ca^{2+}
360 amplitude for individual calcium transients was determined from baseline to peak. In all figures,
361 symbols show the mean and the error bars indicate the SEM.

362

363 *Non-stationary single compartment model of presynaptic Ca^{2+} dynamics*

364 Experimental Ca^{2+} fluorescence traces were analysed using a non-stationary single compartment
365 model^{9,10}, which assumes spatial homogeneity of $[Ca^{2+}]$ in the nerve terminal. The model is
366 described by the following system of differential equations:

$$\frac{d[Ca^{2+}]}{dt} = j_{Ca} + k_{off}^I [CaI] - k_{on}^I [Ca^{2+}][I] + \sum_i (k_{off}^{B_i} [CaB_i] - k_{on}^{B_i} [Ca^{2+}][B_i]) - P_{rem}$$

$$\frac{d[I]}{dt} = k_{off}^I [CaI] - k_{on}^I [Ca^{2+}][I]$$

$$\frac{d[B_i]}{dt} = k_{off}^{B_i} [CaB_i] - k_{on}^{B_i} [Ca^{2+}][B_i]$$

367

368 where the square brackets denote concentrations, and the superscript indices of the reaction rate
369 constants denote endogenous Ca^{2+} buffers B_i or the Fluo-4FF indicator I . The action potential-

370 dependent Ca^{2+} influx time course j_{Ca} was approximated by the Gaussian function

371
$$j_{\text{Ca}} = \frac{\Delta[\text{Ca}^{2+}]_{\text{total}}}{\sigma\sqrt{2\pi}} \sum_i \exp\left(-\frac{(t-t_i^{\text{AP}})^2}{2\sigma^2}\right)$$
 where t_i^{AP} denotes the times of peaks of Ca^{2+} currents

372 during each action potential. The use of the low affinity Ca^{2+} indicator Fluo-4FF ($K_d = 9.7 \mu\text{M}$)
373 did not allow us to estimate resting $[\text{Ca}^{2+}]_{\text{rest}}$ reliably, which in turn prevented the numerical
374 estimation of the total volume averaged presynaptic Ca^{2+} entry $\Delta[\text{Ca}^{2+}]_{\text{total}}$. Therefore we used
375 previous estimates for both $[\text{Ca}^{2+}]_{\text{rest}} = 75 \text{ nM}$ and $\Delta[\text{Ca}^{2+}]_{\text{total}} = 50 \mu\text{M}$ obtained with high
376 affinity Ca^{2+} indicators^{9,21}. Because in our experimental conditions $[\text{Ca}^{2+}]_{\text{ext}} = 1.2 \text{ mM}$ (in
377 comparison to $[\text{Ca}^{2+}]_{\text{ext}} = 2 \text{ mM}$ in ref.⁹) we reduced $\Delta[\text{Ca}^{2+}]_{\text{total}}$ determined in ref.⁹ by a factor
378 of 1.5 based on the dependency of VGCC conductance on $[\text{Ca}^{2+}]_{\text{ext}}$. Ca^{2+} removal was
379 approximated by a first-order reaction $P_{\text{rem}} = k_{\text{rem}}([\text{Ca}^{2+}] - [\text{Ca}^{2+}]_{\text{rest}})$. We assumed that a MFB
380 terminal contains three endogenous buffers ATP, CB and CaM. The complete set of model
381 parameters and Ca^{2+} binding reactions is specified in **Supplementary Table 1**. The model was
382 numerically solved using the adaptive step-size Runge-Kutta algorithm. The model operated with
383 only two adjustable (free) parameters: the unknown ratio between resting Fluo-4FF fluorescence
384 signal and the background fluorescence and Ca^{2+} removal rate k_{rem} . Both parameters were
385 constrained by a straightforward fitting procedure that would match the calculated and
386 experimental fluorescence profiles.

387

388 *Spatial VCell model of MFB Ca^{2+} dynamics*

389 Three-dimensional modeling of AP-evoked presynaptic Ca^{2+} influx, buffering, and diffusion was
390 performed in the Virtual Cell (VCell) simulation environment (<http://vcell.org>) using the fully
391 implicit adaptive time step finite volume method on a 10 nm meshed geometry. A simulation
392 unit, representing part of a MFB terminal with a single active zone (AZ), was modeled as a
393 parallelepiped of size $x = 0.5 \mu\text{m}$, $y = 0.5 \mu\text{m}$ and $z = 0.79 \mu\text{m}$. The AZ was located in the
394 XY base ($z = 0.79 \mu\text{m}$) and contained a single rectangular VGCC cluster of dimensions
395 40 nm x 80 nm placed in the center of the AZ. The size of XY base corresponded to the average
396 distance among different AZs in MFB terminals ($0.5 \mu\text{m}$)²². The height of the simulation unit

397 was adjusted to $\bar{z} = 0.79 \mu\text{m}$ in order to match the magnitude of local VGCC-mediated Ca^{2+}
398 influx at the AZ (see below) to the value of experimentally estimated $\Delta[\text{Ca}^{2+}]_{\text{total}} = 33.3 \mu\text{M}$. We
399 assumed that 28 VGCCs were evenly distributed within the VGCC cluster^{11,13}. The average AP-
400 evoked Ca^{2+} current was simulated using the five-state VGCC gating kinetic model in MFB¹¹
401 using the NEURON simulation environment^{14,23} and the experimentally determined MFB AP
402 waveform¹¹, which was considered to be constant during burst of APs. Ca^{2+} extrusion by the
403 bouton surface pumps (excluding the AZ) was approximated by a first-order reaction:
404 $j_{\text{extr}} = k_{\text{extr}}([\text{Ca}^{2+}] - [\text{Ca}^{2+}]_{\text{rest}})$ ^{10,24} located at the XY parallelepiped base opposite to the AZ;
405 k_{extr} was calculated using the experimentally constrained single-compartment model average
406 Ca^{2+} removal rate ($k_{\text{rem}} = 400 \text{ s}^{-1}$) as $k_{\text{extr}} = \frac{V}{S} k_{\text{rem}} = 320 \mu\text{m s}^{-1}$ (where V is the volume of the
407 simulation unit and S is the area of the XY base). In the case of ‘Mobile CaM’ model we
408 assumed $[\text{CaM}]_{\text{total}} = 150 \mu\text{M}$ as was estimated in **Supplementary Fig. 8a**. In the case of ‘CaM
409 dislocation’ model we assumed that all CaM molecules were located within a single 10 nm layer
410 of VCell voxels adjacent to the AZ plasma membrane (i.e. at the $0.5 \mu\text{m} \times 0.5 \mu\text{m}$ bottom base of
411 the simulation unit). Concentration of CaM was 3 molecules / $10 \text{ nm} \times 10 \text{ nm} \times 10 \text{ nm}$ voxel, as
412 estimated in **Supplementary Fig. 8c**. The details of ‘CaM dislocation’ model are described in
413 our previous publication (ref. 29). Briefly, we assumed that upon binding of two Ca^{2+} ions by the
414 C-lobe a CaM molecule can irreversibly dissociate from the plasma membrane ($k_{\text{off}}^{\text{CaM}} = 650 \text{ s}^{-1}$,
415 ref. 29) and freely diffuse in the cytosol.

416

417 *Modeling of Ca^{2+} -triggered synaptic vesicle fusion*

418 We assumed that the vesicular Ca^{2+} release sensor was located at coupling distance $d = 90 \text{ nm}$
419 from the edge of VGCC cluster (**Fig. 3a**). To simulate glutamate release we used $[\text{Ca}^{2+}](t)$
420 profiles obtained in VCell at this location for each specific AP firing pattern in Monte Carlo
421 simulations (implemented in MATLAB) based on the six-state allosteric Ca^{2+} sensor model¹²
422 (**Fig. 3c**). The model also contained a stochastic re-priming step, which was preceded by a short
423 refractory period (1 ms) immediately after vesicle fusion. The model parameters were: $k_{\text{on}} = 100$
424 $\mu\text{M}^{-1} \text{ s}^{-1}$, $k_{\text{off}} = 4 \times 10^3 \text{ s}^{-1}$, $b = 0.5$, $f = 31.3$, $I_{+} = 2 \times 10^{-4} \text{ s}^{-1}$. The re-priming rate $k_{\text{rep}} = 20 \text{ s}^{-1}$

425 was constrained using the experimental data for 50 stimuli applied at 100 Hz (**Supplementary**
426 **Fig. 5**). For each stimulation paradigm, we performed 60,000 independent Monte Carlo runs
427 with a time step $dt = 10^{-6}$ s and thus determined distribution for the vesicle fusion time during
428 AP burst. Simulated EPSC response was calculated as $EPSC = m \sum_i qEPSC(t - t_i) / 60,000$,
429 where $m = 125$ is the average RRP size and $qEPSC(t)$ is the average quantal EPSC which was
430 determined using voltage-clamp recoding during the asynchronous phase of release (200 – 300
431 ms after the last AP in the burst).

432

433

434

435

436

437

438

439

440

441

442

443

444

445

446

447

448

449

450

451

452

453

454

455

456

457

458 **Bibliography for Online Methods**

459 19 Bischofberger, J., Engel, D., Li, L., Geiger, J. R. & Jonas, P. Patch-clamp recording from
460 mossy fiber terminals in hippocampal slices. *Nature protocols* **1**, 2075-2081,
461 doi:10.1038/nprot.2006.312 (2006).

462 20 Otsu, Y. *et al.* Optical monitoring of neuronal activity at high frame rate with a digital
463 random-access multiphoton (RAMP) microscope. *Journal of neuroscience methods* **173**,
464 259-270, doi:10.1016/j.jneumeth.2008.06.015 (2008).

465 21 Jackson, M. B. & Redman, S. J. Calcium dynamics, buffering, and buffer saturation in
466 the boutons of dentate granule-cell axons in the hilus. *The Journal of neuroscience : the*
467 *official journal of the Society for Neuroscience* **23**, 1612-1621 (2003).

468 22 Rollenhagen, A. *et al.* Structural determinants of transmission at large hippocampal
469 mossy fiber synapses. *The Journal of neuroscience : the official journal of the Society for*
470 *Neuroscience* **27**, 10434-10444, doi:10.1523/JNEUROSCI.1946-07.2007 (2007).

471 23 Hines, M. L. & Carnevale, N. T. The NEURON simulation environment. *Neural*
472 *computation* **9**, 1179-1209 (1997).

473 24 Matveev, V., Bertram, R. & Sherman, A. Residual bound Ca²⁺ can account for the
474 effects of Ca²⁺ buffers on synaptic facilitation. *Journal of neurophysiology* **96**, 3389-
475 3397, doi:10.1152/jn.00101.2006 (2006).

476

477

478

479

480

481

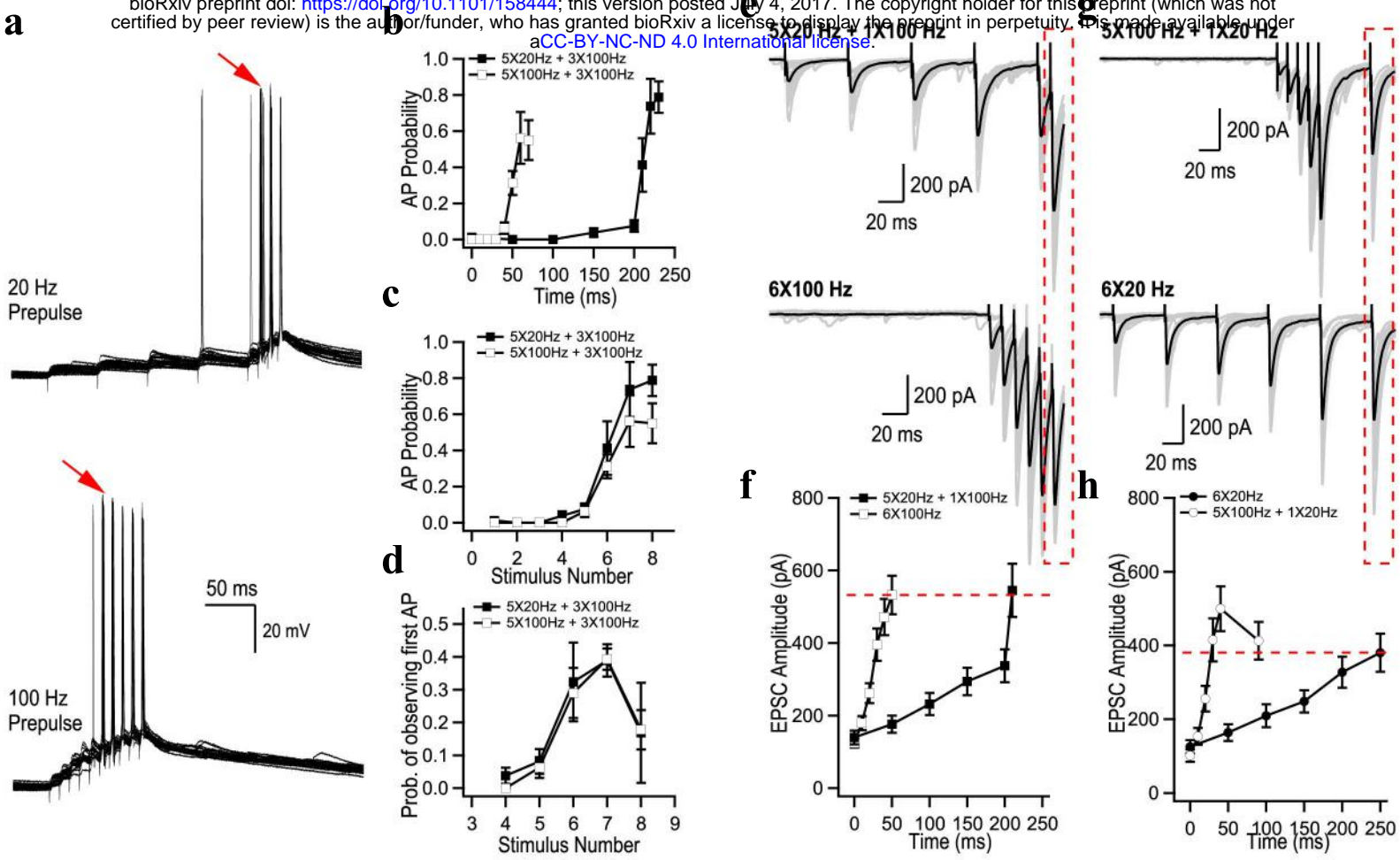


Figure 1

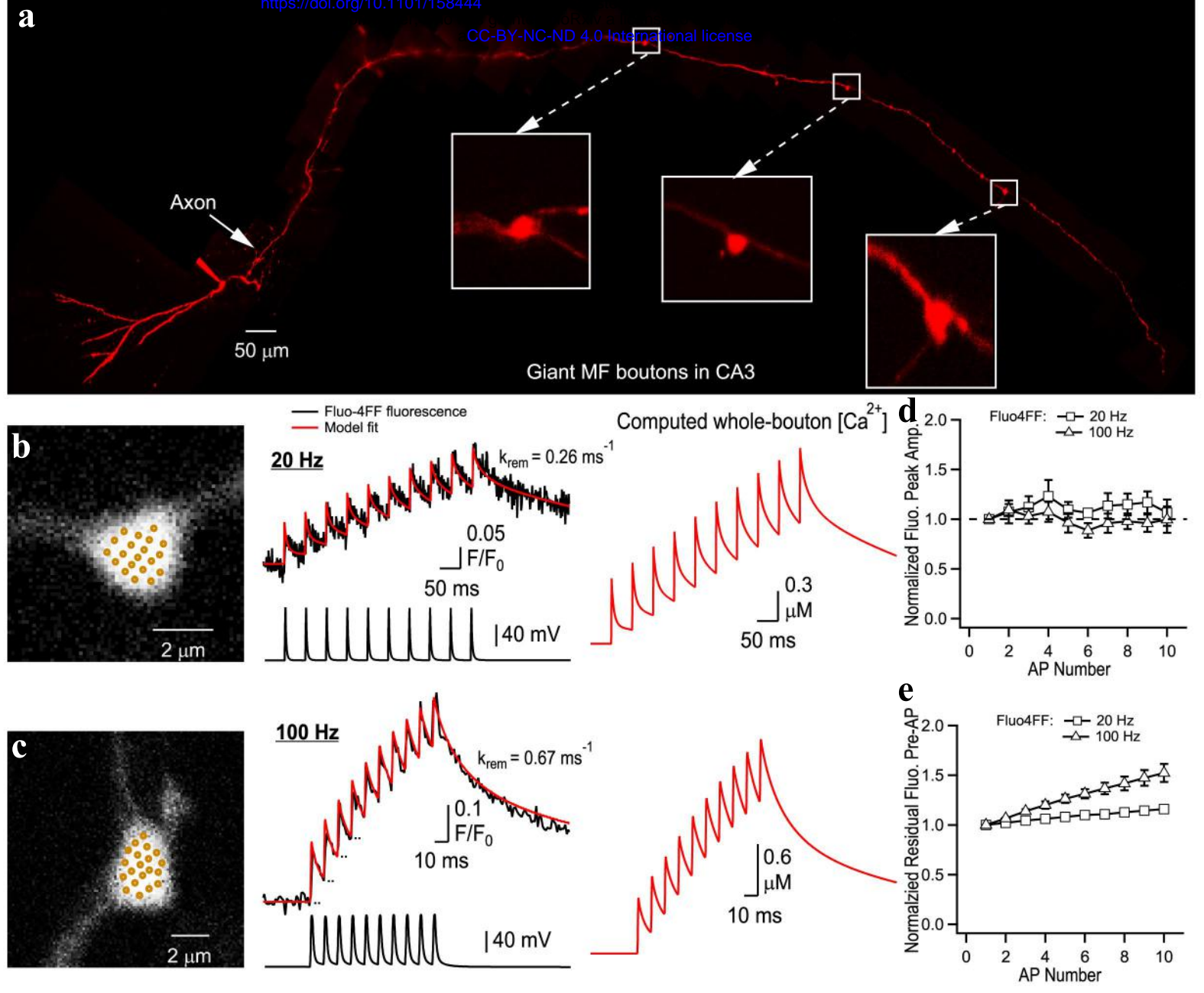


Figure 2

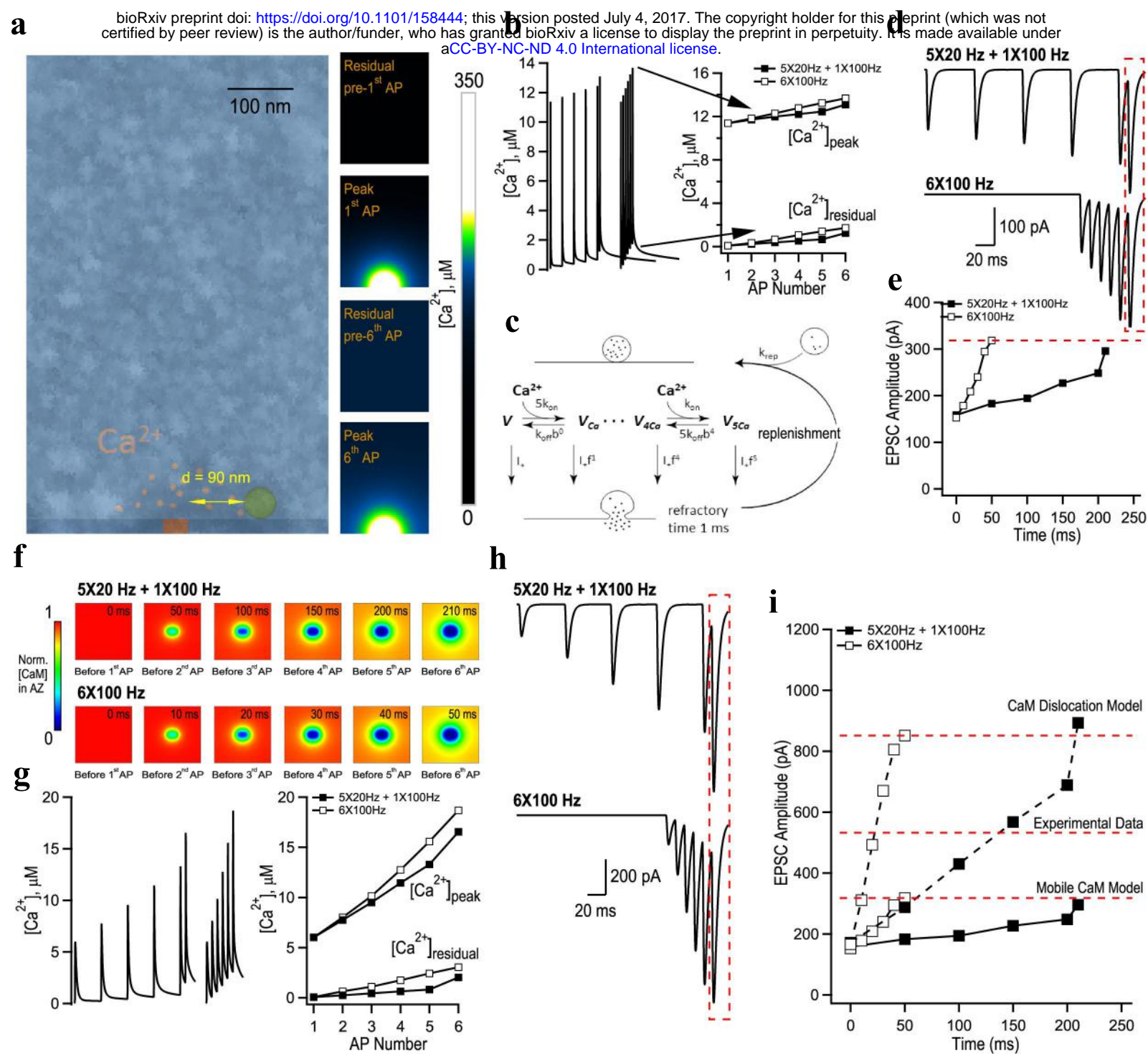


Figure 3